

## Article

# Synthesis and Characterization of Epoxy-Rich TMOs Deposited on Stainless Steel for Corrosion Applications

Atzin Ferrel-Alvarez <sup>1</sup>, Brenda B. Galicia <sup>2</sup>, Adhikari Ashok <sup>1,2</sup>, Ganesh Regmi <sup>1</sup>, Subramaniam Velumani <sup>1,2</sup>   
and Homero Castaneda <sup>2,\*</sup> 

<sup>1</sup> Department of Electrical Engineering (SEES), Centro de Investigación y de Estudios Avanzados del Instituto Politécnico Nacional (CINVESTAV-IPN), Av. Instituto Politécnico Nacional 2508, Col. San Pedro Zacatenco, Mexico City 07360, Mexico; atzin.ferrel@gmail.com (A.F.-A.); ashokad12@tamu.edu (A.A.); ganesh@cinvestav.mx (G.R.); velu@tamu.edu (S.V.)

<sup>2</sup> Department of Materials Science and Engineering, National Corrosion and Materials Reliability Laboratory, Texas A&M University, College Station, TX 77840, USA; bren\_galam\_15@tamu.edu

\* Correspondence: hcastaneda@tamu.edu; Tel.: +1-979-458-9844

**Abstract:** Epoxy-trimetallic oxide (epoxy-TMO) coatings of ZrO<sub>2</sub>:TiO<sub>2</sub>:ZnO at different compositions were synthesized and used to protect a stainless steel surface. The different TMO compositions were synthesized using the ball-milling method and later dispersed on the polymer matrix. The different characterizations performed on these coatings showed that the epoxy-TMO coating with a ratio of 50:40:10 (wt%) exhibited the highest corrosion resistance, in the order of  $\sim 10^{12}$  Ωcm<sup>2</sup>, due to the barrier effect of the distributed particles after 28 days in an aggressive environment (3.5 wt% NaCl solution). The influence of the metal oxides in forming a semiconductor layer produces a capacitor-like behavior, influencing corrosion control via a mass transfer mechanism barrier. The water uptake reveals the effect of each metal oxide in the formation of a physical barrier due to the dispersion mechanism, as well as how the particles function within the polymer matrix.

**Keywords:** ZrO<sub>2</sub>:TiO<sub>2</sub>:ZnO; epoxy coatings; nanocomposite reinforcement; UV resistance; wettability; corrosion resistance



**Citation:** Ferrel-Alvarez, A.; Galicia, B.B.; Ashok, A.; Regmi, G.; Velumani, S.; Castaneda, H. Synthesis and Characterization of Epoxy-Rich TMOs Deposited on Stainless Steel for Corrosion Applications. *Coatings* **2022**, *12*, 387. <https://doi.org/10.3390/coatings12030387>

Academic Editor: Ingrid Milošev

Received: 8 February 2022

Accepted: 9 March 2022

Published: 15 March 2022

**Publisher's Note:** MDPI stays neutral with regard to jurisdictional claims in published maps and institutional affiliations.



**Copyright:** © 2022 by the authors. Licensee MDPI, Basel, Switzerland. This article is an open access article distributed under the terms and conditions of the Creative Commons Attribution (CC BY) license (<https://creativecommons.org/licenses/by/4.0/>).

## 1. Introduction

Stainless steel (SS) is widely used in industry due to its excellent corrosion resistance and low cost. However, this material tends to suffer localized corrosion due to the breakdown of the passivation layer formed on the steel surface [1]. Organic coatings are the most widely applied method for corrosion protection of metallic materials, providing a protective barrier and preventing the diffusion of oxygen and water through the insulating layer [2]. Among organic coatings, epoxy resins are the most used polymers in the protection of steel, due to their excellent physical and chemical properties—such as adhesion, chemical resistivity, and mechanical and dielectric properties [3]—and they are widely used for industrial applications such as aerospace parts, electrical laminates, and construction materials [4]. However, like all polymers, they are susceptible to corrosive species such as oxygen, aggressive ions, and water molecules at the metal-coating interface, reducing the coating adhesion and facilitating corrosion of the metal underneath the film [5,6]. However, incorporating inorganic nanoparticles can improve the barrier properties and protective performance of the epoxy coatings. Different inorganic materials, including silicon oxide (SiO<sub>2</sub>), titanium dioxide (TiO<sub>2</sub>), zinc oxide (ZnO), cerium oxide (CeO<sub>2</sub>), and zirconium oxide (ZrO<sub>2</sub>), among others, are recognized as excellent candidates for their physical and mechanical properties, owing to their grain size and grain boundary volume [7]. There are different types of applicator—such as brush, airbrush, doctor blade, drop-casting, dip-coating, spin-coating, etc.—for applying the epoxy coatings to the metallic surface [8].

Individual oxides of Zr, Zn, and Ti are commonly used for corrosion-resistant coatings, and present good performance. However, the use of single oxides exhibits some flaws, due to pores and cracks in the coatings. Conversely, a hybrid or mixed metal oxide coating can potentially combine the intrinsic properties of all of the metal oxides, improving the adherence and enhancing the barrier to dissemination and preclusion of charge transport. The properties of the coatings can be tailored by controlling the concentrations of each metal oxide nanoparticle to overcome the limitations of a single metal oxide [9,10].

This study proposes a novel and hybrid combination of ZrO<sub>2</sub>, TiO<sub>2</sub>, and ZnO nanoparticles at different ZrO<sub>2</sub>-richness ratios using the ball-milling technique, and added to a commercial epoxy resin intended to achieve anticorrosive properties. The extensive work was applied on a previously reported highly resistive TMO coating also synthesized via the ball-milling method. This synthesis method uses mechanical energy to activate chemical reactions and structural changes, and is able to reduce the particle size [11]. These TMO nanoparticles were deposited by RF magnetron sputtering as a multifunctional (self-healing, anticorrosive, antireflective, and self-cleaning) layer [12]. For the first time, we present a systematic fundamental analysis of the different nanoparticles' ratios in the epoxy matrix, with a minimum wt%, in order to determine the efficacy in the corrosion protection properties on SS substrates.

## 2. Materials and Methods

### 2.1. Synthesis of the Trimetallic Oxide Compounds

The three different oxides (ZrO<sub>2</sub>, TiO<sub>2</sub>, and ZnO; Sigma-Aldrich, Mexico) were weighed and mixed at different enriched ZrO<sub>2</sub> proportions, forming six different compositions of TMOs, as shown in Table 1. All of the mixed TMOs were annealed at 700 °C for 2 h in a non-vacuum oven and mechanically milled at 300 rpm for 3 h. Finally, the TMO nanocomposites were sintered at 700 °C for 2 h in order to increase the density of the different oxides and the formation of the metalloids [13].

**Table 1.** Composition of trimetallic oxides (wt%).

TMO	ZrO <sub>2</sub>	TiO <sub>2</sub>	ZnO
A	90	5	5
B	80	10	10
C	65	25	10
D	50	40	10
E	40	50	10

The epoxy-TMO coatings were prepared using commercial epoxy resin (Grupo Imperquimia, Mexico City, Mexico) mixed with the different TMO compositions at proportions of epoxy resin at 99 wt% and TMO at 1 wt%, using magnetic stirring for 15 min. After that, the commercial hardener was added to the mixture to obtain a 60:40 wt% ratio of epoxy-catalyst mixed by magnetic stirring for 3 min and sonicated in deionized water to release trapped air bubbles inside the coating. The resulting epoxy-TMO coatings were deposited on the SS 430 metallic substrates by drop-casting, repeating this procedure to obtain uniform coatings controlled by a doctor blade, with average wet thicknesses of 100 µm. After that, the resulting coatings were dried at room temperature for 24 h and measured with a thickness measurer, obtaining an average thickness of the coatings between 60 and 80 µm.

### 2.2. Characterization

The crystal structure of the synthesized TMOs was characterized by X-ray diffraction (XRD, Bruker, Massachusetts, United States) with a copper K $\alpha$  radiation source ( $\lambda = 1.5405 \text{ \AA}$ ), at a scan rate of  $0.04^\circ \text{ min}^{-1}$ , using a Bruker AXS D8 Advanced apparatus. The oxides were analyzed in the  $2\theta$  range from  $10^\circ$  to  $80^\circ$ . The morphology and

composition of the TMOs were studied using a TESCAN Vega3 SEM (TESCAN Company, Brno, Czech Republic) fitted with a Bruker EDS and an Olympus America DXS 500 optical microscope. Raman analysis was performed using NT-MDT NTEGRA spectra, with a shift in the range of 300 to 3300  $\text{cm}^{-1}$ . The optical absorbance of the coated films was characterized using a JASCO V-670 spectrophotometer in the wavelength between 200 and 600 nm, and the water contact angle was measured using Data Physics (OCA 35, dataphysics instruments, Filderstadt, Germany) with 4  $\mu\text{L}$  of distilled water.

The electrochemical behavior of the coatings was assessed in a 3.5 wt% NaCl solution at room temperature for various immersion times (i.e., from 1 to 28 days). The measurements were performed with a potentiostat/galvanostat (Gamry Instruments REF600<sup>®</sup> potentiostat, Gamry Instruments, Warminster Pennsylvania, United States). A typical three-electrode setup was used: the coated SS substrate as the working electrode, with an exposed area of 2.714  $\text{cm}^2$ , a saturated calomel electrode (SCE) as the reference electrode, and a platinum grid wire as a counter electrode. Electrochemical techniques such as open-circuit potential ( $E_{\text{OCP}}$ ), electrochemical impedance spectroscopy (EIS), and linear polarization resistance (LPR) were performed using a Gamry REF600<sup>®</sup> potentiostat. EIS measurements were carried out at  $E_{\text{OCP}}$  with a sinusoidal potential of 10 mV in amplitude. The frequency range was observed from  $10^5$  to  $10^{-2}$  Hz, with 10 points per decade interval. The corrosion behavior of the commercial epoxy coating was also tested under the same conditions, providing a baseline for coating evaluation.

### 3. Results and Discussion

#### 3.1. XRD

XRD patterns of TMO nanocomposites depict their polycrystalline nature, with a significant presence of multiple peaks corresponding to mixed metal oxide phases, indicating the metallization during the nanocomposite formation [12]. Figure 1 shows the XRD spectra of the TMO nanoparticles. The XRD results present the characteristic  $2\theta$  peak values at  $\sim 16.7^\circ$ ,  $24.3^\circ$ , and  $43^\circ$ , corresponding to the monoclinic phase of  $\text{ZrO}_2$ , with the prominent peak at  $2\theta = 28.6^\circ$  belonging to the  $(-111)$  plane (ICDD 00-065-0728) [14]. With an increase in the content of  $\text{TiO}_2$ , the intensity of tetragonal anatase  $\text{TiO}_2$  (ICDD 01-070-2556) is enhanced, whereas the intensity of  $\text{ZrO}_2$  is reduced [15].

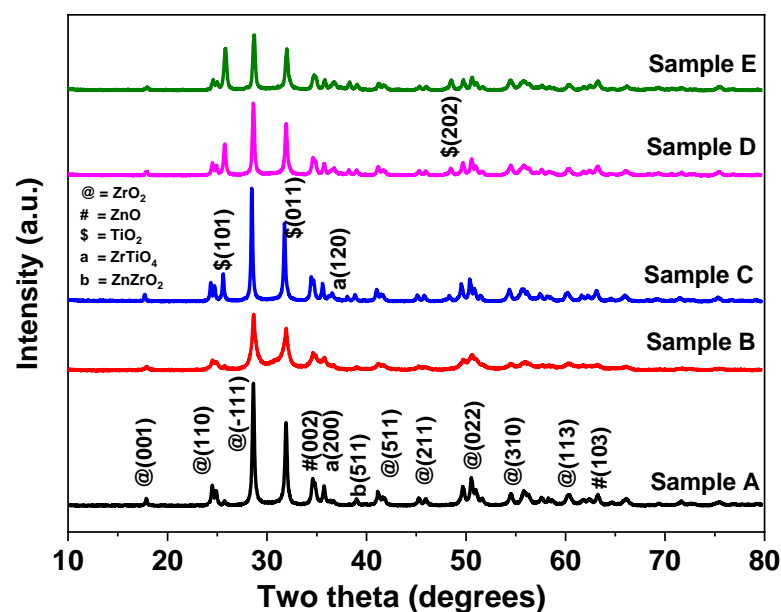


**Figure 1.** XRD spectra of the sintered TMO ( $\text{ZrO}_2\text{:TiO}_2\text{:ZnO}$ ) nanoparticles, ball-milled and annealed at  $700^\circ\text{C}$ .

The observed peak at  $2\theta = 34.4^\circ$  corresponding to the (002) plane suggests the presence of hexagonal ZnO (ICDD 01-082-9744) [16]. A small peak can also be found at a  $2\theta$  value of around  $40^\circ$ , corresponding to the (511) plane of the  $\text{ZnZrO}_2$ , confirming the formation of the mixed metal oxide phase.

The average crystallite size (Table 2) for each oxide was calculated with the Debye-Scherrer equation, using diffraction angle and peak full width at half-maximum (FWHM):

$$D = \frac{0.94\lambda}{\beta \cos\theta} \quad (1)$$

where  $D$  is the crystallite's average size,  $\lambda$  is the wavelength of the X-ray radiation,  $\beta$  is the peak FWHM in radians, and  $\theta$  is the diffraction peak position.

**Table 2.** Average crystallite size of the TMO oxides.

TMO	ZrO <sub>2</sub> (nm)	TiO <sub>2</sub> (nm)	ZnO (nm)	ZrTiO <sub>4</sub> (nm)	ZnZrO <sub>2</sub> (nm)
A	12	21	26	37	35
B	12	15	19	35	34
C	18	17	19	45	34
D	27	16	17	44	31
E	26	16	17	41	34

The crystallite sizes of ZrO<sub>2</sub> varied between 12 and 27 nm, depending on the content of the entire composite, as shown in Table 2. The crystallite size of ZrO<sub>2</sub> for samples A to C was smaller than for samples D and E. This result shows that decreasing the quantity of ZrO<sub>2</sub> in the TMO composite enhances the crystallinity of the nanoparticles. The average crystallite size varied between 35 and 44 nm for the ZrTiO<sub>4</sub>, indicating enhancement in crystallinity with increasing TiO<sub>2</sub> content in the composite. The crystallinity of ZnZrO<sub>2</sub> does not depend on the quantity of ZrO<sub>2</sub>, as was verified by the constant crystallite size of composite ZnZrO<sub>2</sub> for all of the samples.

### 3.2. Morphological Characterization

The SEM micrograph of the TMO powders shows agglomeration of the nanoparticles with a random distribution of the constituent elements, with a grain size ranging between 130 and 500 nm; this could be due to the annealing process after the ball-milling synthesis provoking the increase in the particle size of the TMOs [17] (Figure 2a). Velumani et al. [12] synthesized this TMO via ball-milling and obtained an average grain size between 92 and 106 nm with decreasing ZrO<sub>2</sub> content, including the formation of agglomerates. Figure 2b shows a micrograph where the thickness of the epoxy sample measured from the cross-section was  $\sim 70 \mu\text{m}$ , with no observation of significant agglomeration of the TMO nanoparticles within the epoxy coating.

The elemental composition of the epoxy-TMO coatings is shown in Table 3. The proportion between the epoxy coating and the TMO was small, and it was not possible to observe in the elemental mapping. We also observed that elements such as iron (Fe) and chromium (Cr) may correspond to the substrate and the content of carbon content from the epoxy material.

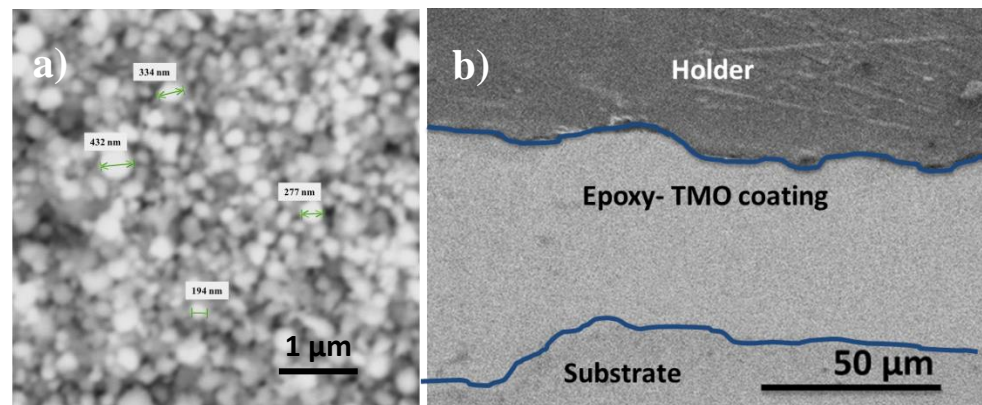


**Figure 2.** (a) SEM micrograph of TMO ( $ZrO_2:TiO_2:ZnO$ ); (b) cross-section SEM images of epoxy-TMO coatings on an SS substrate.

**Table 3.** Elemental composition for a cross-section image of the epoxy films with different trimetallic oxide compositions.

Samples	C (%)	O (%)	Zr (%)	Zn (%)	Ti (%)	Cr (%)	Fe (%)
A	83.82	8.97	2.85	0.69	0.59	0.76	2.32
B	86.42	5.19	3.22	0.90	1.24	0.92	2.11
C	86.91	5.91	2.15	1.04	1.45	0.63	1.91
D	82.68	6.85	2.23	0.47	1.33	2.24	4.20
E	82.88	7.38	1.54	0.53	1.61	2.93	3.13

### 3.3. Raman Analysis

Figure 3 shows Raman analysis of the epoxy-TMO to determine whether the phases (wurtzite ZnO and monoclinic  $ZrO_2$ ) characterized by XRD as being present in the coatings maintain their phases after annealing at 700 °C [18]. The observed peaks at 1120 and 1620  $cm^{-1}$  correspond to the benzene ring quadrant stretching characteristics of the epoxy ring vibration; the signal at 830  $cm^{-1}$  could also be related to the vibrations of the entire epoxy ring (i.e., characteristic of the  $CH_2$  epoxy asymmetric, and vibration of the C-H groups of the epoxy ring) [19]. The absence of peaks of TMO oxides (1 wt%) may be due to their small amount, which is insufficient to exhibit significant peaks in the Raman modes corresponding to the present oxides.

### 3.4. Optical Analysis of Epoxy-Rich Coatings

The epoxy systems have significant chemical and mechanical properties; they possess aromatic groups with strong absorption in the UV range at 300 nm, making the epoxy structures susceptible to photodegradation. UV light forms free radicals on the surface of the polymer, and is highly active in attacking the polymer structures. Other environmental factors—including humidity, oxygen, temperature, and pollutants—can decrease the lifetime of the polymer. Thus, added inorganic nanoparticles such as ZnO and  $TiO_2$  scatter the light, and have broad absorption in the UV range, while they have almost no absorption in the visible range [20]. The absorbance and transmittance plots for the coatings (Figure 4) showed two characteristic absorption peaks of the epoxy resin at ~280 and ~350 nm.

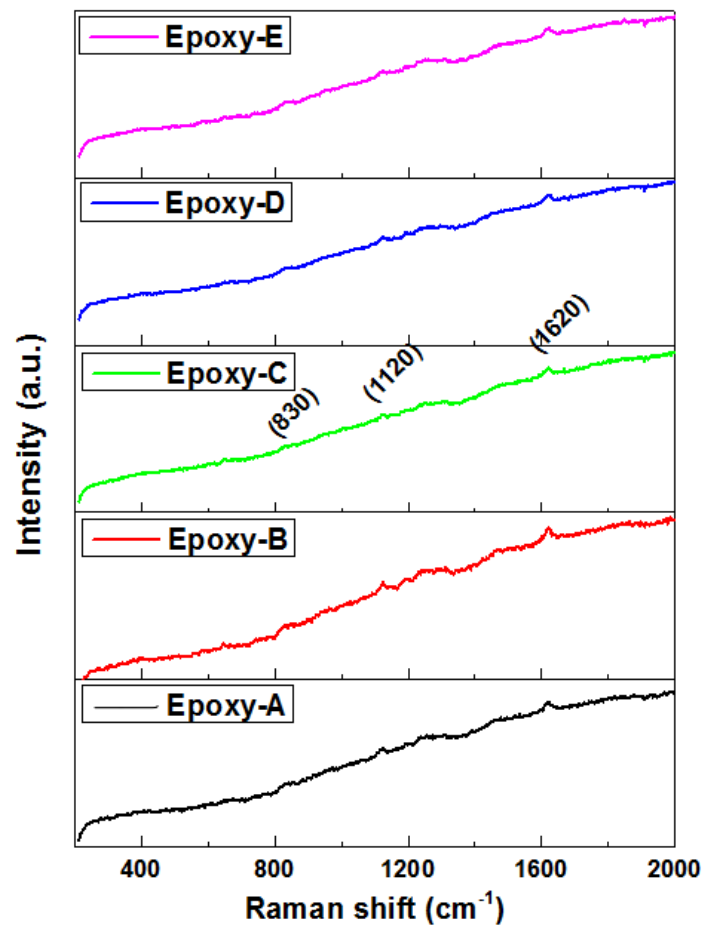


Figure 3. Raman spectra of the epoxy-TMO coatings at different ratios of  $ZrO_2:TiO_2:ZnO$ . Epoxy-A (90:5:5), Epoxy-B (80:10:10), Epoxy-C (65:25:10), Epoxy-D (50:40:10), Epoxy-E (40:50:10).

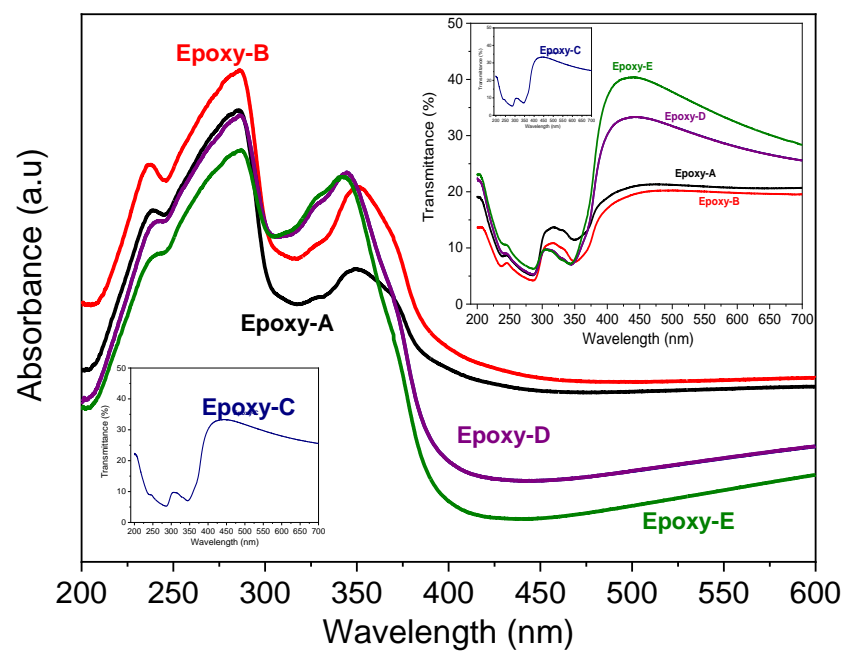


Figure 4. UV absorbance of the synthesized epoxy-TMO ( $ZrO_2:TiO_2:ZnO$ ) coatings: Epoxy-A (90:5:5), Epoxy-B (80:10:10), Epoxy-C (65:25:10), Epoxy-D (50:40:10), Epoxy-E (40:50:10).

The epoxy systems have significant chemical and mechanical properties. From the transmittance plot, it can be seen that they possess aromatic groups with strong absorption. All of the coatings presented low transmittance, reaching a maximum of 50%, showing the capacity of the coating to absorb light due to the properties of the different oxides in the TMOs. Incorporating TiO<sub>2</sub> nanoparticles within the epoxy coating tends to broaden the absorption region of the epoxy resin and enhance the absorption intensity at around 250 nm within the TiO<sub>2</sub> absorption range. Thus, the UV range is enhanced by incorporating this oxide, as observed in Figure 4 for the deposited coatings [21]. This enhancement may be due to TiO<sub>2</sub>, which has a wide bandgap of ~3.2 eV, and tends to absorb the shorter wavelength with high energy to excite its electrons below 400 nm, where it does not have a specific peak within this region. The absorption range of nano-ZnO reported between 360–230 nm can also block the UV radiation in organic coatings [22] and observed at ~246 nm.

Xu et al. [23] reported that TiO<sub>2</sub>/ZnO composites presented stronger photoabsorption than pure ZnO and TiO<sub>2</sub>. The absorption edge of TiO<sub>2</sub>/ZnO showed a redshift to the visible spectrum range, ascribed to better scattering of the induced electron-hole pairs in the porous architecture, as well as the mixture effect of the bandgap of the composite semiconductor improving the photoelectric effect of the composite films, and further enhancing the photocathodic properties of the stainless steel substrate.

ZrO<sub>2</sub> presents excellent chemical and physical properties, with a wide bandgap larger than 5 eV, which is crucial in a luminescent material; its good optical transparency makes it a potential candidate for photocatalytic applications due to its high surface area and numerous oxygen vacancies. The monoclinic phase appears more stable at room temperature, depending on the different synthesis parameters, with a reported absorption signal ~204 nm [24]. In the epoxy-TMO, the signal is not observed within these ranges. The signal corresponding to an interaction between ZnO and ZrO<sub>2</sub> is observed at ~246 nm, decreasing with the reduction in the ZrO<sub>2</sub> ratio in the coatings. Sathyaseelan et al. [25] reported absorption peaks at 215 and 217 nm for synthesized and calcined samples of ZrO<sub>2</sub> due to the Zr<sup>+4</sup> ions' d transition. The nanoparticles also showed a weak absorption band at 310 nm due to mid-gap trap sides, such as surface defects and oxygen vacancies. The surface modification resulted in a sharp increase in absorption by the ZrO<sub>2</sub> within the visible region.

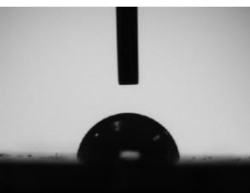
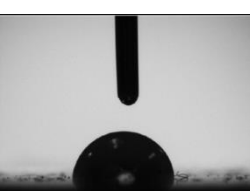
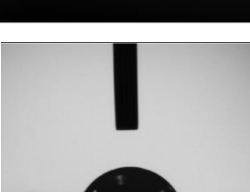
### 3.5. Contact Angle Measurement

Water contact angle (CA) measurements were carried out for the epoxy-TMO coatings to investigate the coated surfaces' wettability state and determine the effects of the different oxides on the coated systems (Table 4). For the epoxy samples, it was not possible to determine a contact angle, and for the epoxy coatings with the nanoparticles, there were differences in the CA. However, the trend showed no significant variation of the contact angle with the decrease in ZrO<sub>2</sub>. All of the epoxy coatings presented hydrophilic characteristics close to 90° except for the epoxy-D coating, which presented a CA of ~73.8° and, compared to the other coatings, exhibited more hydrophilic characteristics. In comparison, the reported CA values for ZrO<sub>2</sub> and ZnO were 67° and 75°, respectively [26].

For these epoxy-TMO coatings, there are two factors related to reducing the water contact angle: the first is the characteristics and properties of the trimetallic nanoparticles; the second is the surface roughness and porosity of the coating. ZrO<sub>2</sub> has the property of increasing the contact angle, reducing the wettability of the material [27]. TiO<sub>2</sub> shows a self-cleaning action related to its photocatalytic activity. The relationship between TiO<sub>2</sub> and hydrophilicity is that the water molecules are chemisorbed on the TiO<sub>2</sub> surface. These water molecules further absorb water via physisorption (van der Waals forces or hydrogen bonds). The physisorbed water molecules act as barriers to prevent close contact between the surface and pollutants. The combination of TiO<sub>2</sub> with ZnO improves the hydrophilicity due to the formation of surface oxygen vacancies [28]. Sanu et al., further explained that reducing the contact angle can also reduce Ti<sup>+4</sup> cations to a Ti<sup>+3</sup> state, and oxidation of O<sup>2-</sup> anions expels some oxygen atoms. When the surface is exposed to moisture, the OH

molecules are physisorbed to the vacancy sites, and the adsorbed OH groups on the surface can convert the surface into a hydrophilic one by creating a sheet of chemisorbed H<sub>2</sub>O through van der Waals forces that block the close contact between the surface and adsorbed contaminants. Thus, the dirt absorbed on the film's surface can be quickly detached using water spread on the surface, showing a self-cleaning effect [29].

**Table 4.** Contact angle measurements of epoxy-TMO coatings.

Sample	Thickness ( $\mu\text{m}$ )	Contact Angle	Drop Image
Epoxy	340	NA	
Epoxy-A	270.8	$85.7 \pm 0.4$	
Epoxy-B	253.9	$81.2 \pm 0.3$	
Epoxy-C	271.2	$84.6 \pm 0.4$	
Epoxy-D	292.5	$73.8 \pm 0.3$	
Epoxy-E	302.6	$81.9 \pm 0.3$	

### 3.6. Electrochemical Characterization

EIS spectra illustrate the interfacial characterization over time based on the coating composition. Figure 5a–c display the three EIS signatures (Nyquist, Bode, and phase angle,

respectively) for the epoxy and epoxy-TMO compositions following 21 days of 3.5 wt% NaCl, exposure where the representative values of this interface display high resistance.

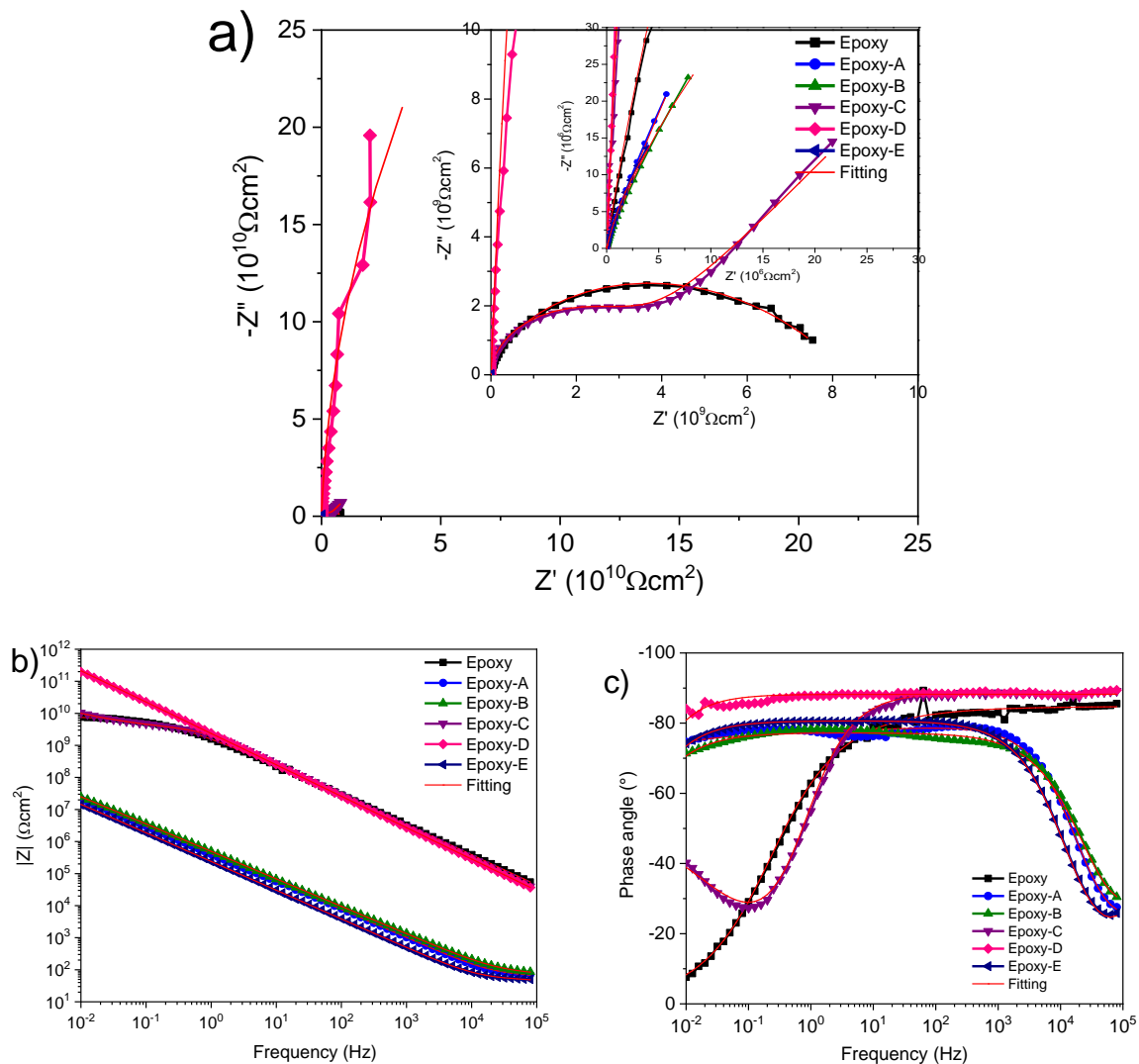


**Figure 5.** (a) Nyquist, (b) Bode, and (c) phase angle plots of the epoxy and epoxy-TMO coatings at day 21.

The classic water uptake process occurring in a polymeric matrix coating [30] prevails during the early stages, achieving resistances in the order of  $10^6$ – $10^{11}$   $\Omega\text{cm}^2$ . The semicircle or loop shape of the complex representation resembles the epoxy's evolution in terms of typical charge transfer and capacitance due to the mentioned water uptake within the matrix. The coating has a finite impedance magnitude marked by the loop magnitude ( $\sim 80 \times 10^9$   $\Omega\text{cm}^2$ ). For the epoxy-TMO coatings, epoxy-A illustrates a finite impedance magnitude, with a high magnitude. The complex representation shows capacitive characteristic mechanisms due to the electrolyte uptake; the TMO configuration 95:5:5 ( $\text{ZrO}_2$ : $\text{TiO}_2$ : $\text{ZnO}$ ) confers barrier properties to the polymer matrix. Individually, each oxide provides corrosion protection. For instance, epoxy coatings with  $\text{TiO}_2$  nanocrystals at 1 wt% showed a maximum corrosion resistance of  $10^4$   $\Omega\text{cm}^2$  for these scratched coatings immersed for 18 days in 3.5 wt% NaCl [31]. Xavier J. et al. [32] synthesized epoxy- $\text{ZrO}_2$  coatings at 10 wt% that, after 15 days of immersion in the same electrolyte, obtained a maximum resistance in the order of  $10^5$   $\Omega\text{cm}^2$ . Finally, Rostami et al. [33] synthesized epoxy coatings with 4 wt% ZnO after exposure to the same aggressive environment for 30 days; after 30 days, the coating achieved a maximum resistance in the order of  $10^8$   $\Omega\text{cm}^2$ .

The results observed in the literature prove the efficiency of the combination of these three nanoparticles in improving the corrosion resistance of the coatings. It is well known that the addition of  $\text{TiO}_2\text{:ZrO}_2$  permits the formation of a physical barrier.  $\text{TiO}_2$  is used in pigments to block electrolyte transport. With the addition of  $\text{ZrO}_2$ , there is a reduction in the ionic species reaching the bulk of the polymer, where the particles are distributed in the polymer matrix [34,35].

A higher percentage of  $\text{TiO}_2$  gives similar properties to the previous epoxy composition. The epoxy-B formulation shows controlled water uptake with a capacitive-like behavior due to the higher impedance, similar to epoxy-A, with the phase angle in both cases (epoxy-A and -B) appearing identical, along with the frequency range. Epoxy-C contains no higher concentration of  $\text{TiO}_2$  and  $\text{ZnO}$ , but a decrease in the  $\text{ZrO}_2$  concentration. The results following 21 days present a change in the transport mechanism and an increase in the impedance magnitude. The Nyquist (or complex) plot (Figure 5a) presents a diffusion signature characteristic of the mass transport control process at low frequencies. The higher concentration of  $\text{TiO}_2$  influences the particle distribution within the matrix, as well as the transport mechanism.

From Figure 5a–c, the observed impedance data of the hybrid coatings were analyzed by fitting them to an equivalent circuit model used to yield information on the corrosion mechanism and/or corrosion rate. For these coatings, it is essential to note that the epoxy-D coating with a proportion of 50:40:10 ( $\text{ZrO}_2\text{:TiO}_2\text{:ZnO}$ ) is the one with the highest resistance, reaching values close to  $10^{12} \Omega\text{cm}^2$ , with an ideal capacitance behavior and an infinite real impedance as presented in the equivalent circuit proposed in Figure 6a, while the other epoxy-TMO coatings present the equivalent circuit shown in Figure 6b.

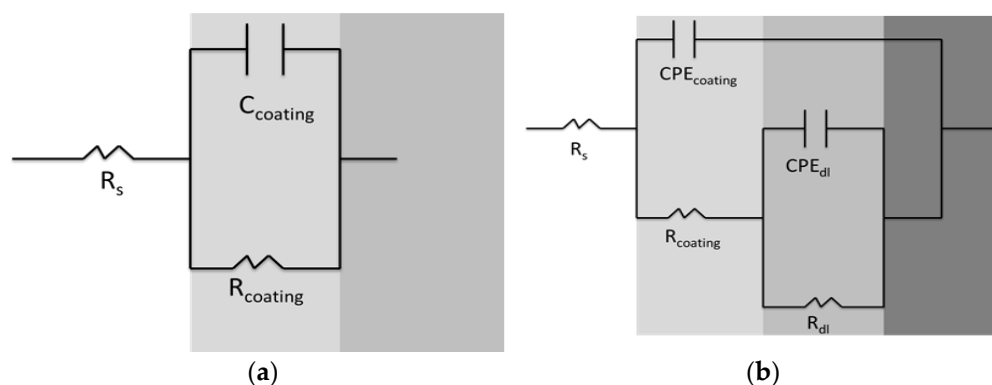


**Figure 6.** Electrochemical equivalent circuit proposed to model impedance data: (a) epoxy-D coating, and (b) other samples.

During the simulation, a constant-phase element (CPE) was used instead of an ideal capacitor to account for the deviations from ideal behavior. The impedance of a CPE ( $Z_{\text{CPE}}$ ) can be defined by  $Z_{\text{CPE}} = (1/Y)(j\omega)^{-\eta}$ , where  $\omega$  is frequency,  $Y$  is pseudo-capacitance, and  $\eta$  is associated with the system homogeneity; when this equation describes a capacitor,  $\eta = 1$  and  $Y = C$  (capacitance).

The fitted data were acquired considering  $\chi^2 < 10^{-3}$ , as observed in Table 5. This information suggests that, in the case of epoxy-D, there is a dielectric barrier blocking any water uptake and electrolyte drainage within the coating during the exposure time, as shown in the corrosion mechanism in Figure 7. The 40 wt%  $\text{TiO}_2$  influences the transport mechanisms within the polymeric coating layer. The formation of an ideal capacitor considers the distribution of particles favoring the physical barrier within the polymer matrix. The semiconductor properties due to the presence of  $\text{TiO}_2$  illustrate the blocking of the ionic species or any electrolytes within the polymer matrix.

**Table 5.** Electrochemical parameters extracted from impedance data for the epoxy and epoxy-TMO coatings immersed in 3.5 wt% NaCl solution for 21 days.

Samples	$R_s$ ( $\Omega\text{cm}^2$ )	$R_{\text{coat}}$ ( $\Omega\text{cm}^2$ )	$Y_{0\text{coat}}$ ( $\text{S} * \text{s}^{\eta}$ )	$\eta$	$Y_{0\text{dl}}$ ( $\text{S} * \text{s}^{\eta}$ )	$\eta$	$R_{\text{ct}}$ ( $\Omega\text{cm}^2$ )	$\chi^2$
Epoxy	101.3	$33.54 \times 10^6$	$77.92 \times 10^{-12}$	0.942	$76.49 \times 10^{-12}$	0.498	$8.43 \times 10^9$	$1.232 \times 10^{-3}$
A	32.60	65.28	$327.5 \times 10^{-9}$	0.811	$167.8 \times 10^{-9}$	0.934	$3.2 \times 10^6$	$959.2 \times 10^{-6}$
B	10	76.77	$39.44 \times 10^{-9}$	0.867	$377.6 \times 10^{-9}$	0.858	$211.2 \times 10^6$	$583.6 \times 10^{-6}$
C	$1.14 \times 10^3$	$3.589 \times 10^9$	$62.55 \times 10^{-12}$	0.984	$633.5 \times 10^{-12}$	0.581	$169 \times 10^9$	$446.1 \times 10^{-6}$
D	100	$1.672 \times 10^{12}$	$69.84 \times 10^{-12}$	1				$699.5 \times 10^{-6}$
E	3.57	48.20	$18.09 \times 10^{-9}$	0.97	$785.8 \times 10^{-9}$	0.894	$114.7 \times 10^6$	$205.4 \times 10^{-6}$

\* means S is multiplied ( $\text{S}(\text{s}^{\eta})$ ).

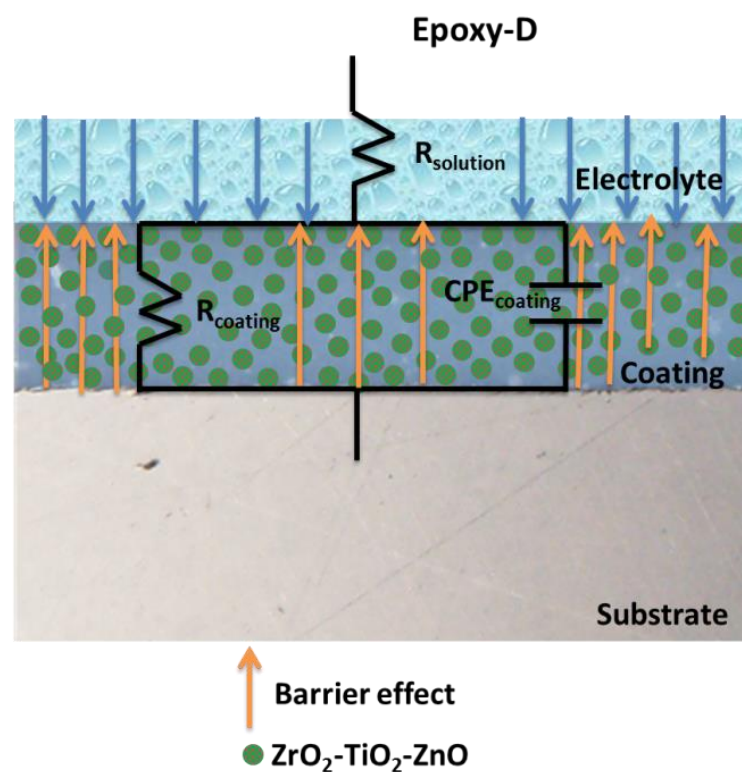


**Figure 7.** Mechanism of corrosion protection of the epoxy-D coating.

The epoxy-TMO coatings presented good resistance behavior by assuming physical barrier protection due to the properties of  $\text{ZrO}_2$  that could present isolator and conductive behavior, and that with the interactions of  $\text{TiO}_2$  and  $\text{ZnO}$ , the coating presents an additional barrier by using the  $\text{TiO}_2$  particles as fillers and blockers. The particle distribution suggests a random distribution within the polymer matrix, and also at the coating surface. The contact angle is clear evidence of the influence of the distribution;  $\text{TiO}_2$  is present at the outmost surface, lowering the contact angle. The contact angle and resistance properties decrease with the increase in  $\text{TiO}_2$ , wetting the surface and taking nothing into the matrix.

Epoxy-D shows a phase angle magnitude close to 90 degrees, while the frequency range and total impedance magnitude reached  $10^{12} \Omega\text{cm}^2$  after 21 days of exposure. The transition of interfacial mechanisms was evident with the increase in  $\text{TiO}_2$  particles, while  $\text{ZrO}_2$  decreased and  $\text{ZnO}$  remained constant. The 90:5:5 ( $\text{ZrO}_2$ : $\text{TiO}_2$ : $\text{ZnO}$ ) ratio showed water uptake with the coating, displaying capacitance and a finite charge transfer process. The transition of interfacial mechanisms was evident with the increase in  $\text{TiO}_2$  particles, while  $\text{ZrO}_2$  decreased and  $\text{ZnO}$  remained constant. The increase in  $\text{TiO}_2$  in the oxide composition 65:25:10 ( $\text{ZrO}_2$ : $\text{TiO}_2$ : $\text{ZnO}$ ) made the mechanism more diffusion-controlled. This was due to a barrier layer influenced by the  $\text{TiO}_2$  particles, and the lower conductivity as a result

of decreasing  $ZrO_2$ . Finally, the highest concentration of  $TiO_2$  (50:40:10,  $ZrO_2:TiO_2:ZnO$ ) produced an ideal capacitance behavior. The particles formed a dielectric layer with no passage of electrolytes, producing an ideal capacitor.

Figure 8a,b present the optical images of the coatings after 28 days of immersion, comparing epoxy-A (Figure 8a) and epoxy-D (Figure 8b), where we can see damage to the interface of the steel substrate, while the epoxy-D does not show visual damage in either the coating or the interface.

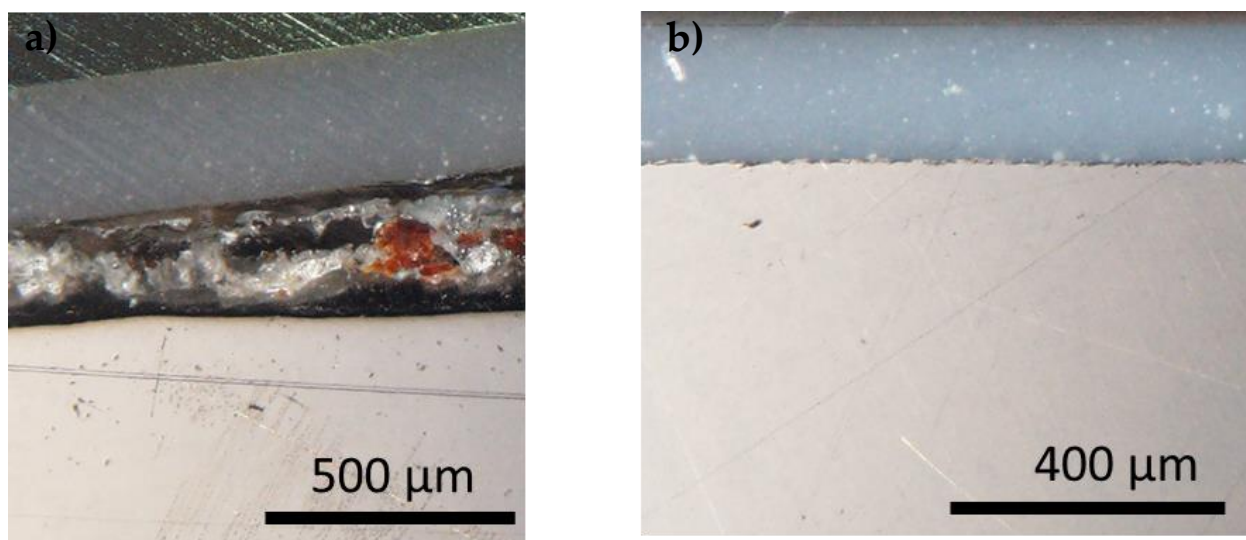


**Figure 8.** (a) Cross-section optical images of (a) epoxy-A and (b) epoxy-D.

Figure 7 presents the protection mechanism of the epoxy-D coating, where it is shown how the integration of the nanoparticles adds an additional barrier layer influencing the electrolyte transport. Mass transport is characteristic of the complex signature and the phase angle format at the lowest frequencies.

Table 6 shows the corrosion resistance rates for different coatings and the metallic substrate at day 21. We can see the decrease in the  $i_{corr}$  with the increase in the  $TiO_2$  and  $ZnO$  and the decrease in  $ZrO_2$  content of the TMOs. We observed that the increase in the  $v_{corr}$  of epoxy-A was consistent with the results obtained in EIS, where the coatings epoxy-C and epoxy-D presented the lowest corrosion rates of  $2.93 \times 10^{-6}$  and  $3.33 \times 10^{-6}$  mpy, respectively.

**Table 6.** Linear polarization resistance (LPR) of the coatings at 21 days.

Sample	$E_{corr}$ (V)	$R_p$ ( $\Omega$ )	$i_{corr}$ ( $A/cm^2$ )	$v_{corr}$ (mpy)
SS	−0.232	$19.95 \times 10^3$	$1.306 \times 10^{-6}$	$219.9 \times 10^{-3}$
Epoxy	−0.117	$938 \times 10^6$	$27.78 \times 10^{-12}$	$4.68 \times 10^{-6}$
Epoxy-A	0.159	$59.81 \times 10^6$	$435.6 \times 10^{-12}$	$73.34 \times 10^{-6}$
Epoxy-B	0.125	$54.51 \times 10^6$	$4.77 \times 10^{-12}$	$80.46 \times 10^{-6}$
Epoxy-C	−0.557	$1.498 \times 10^9$	$17.39 \times 10^{-12}$	$2.93 \times 10^{-6}$
Epoxy-D	−3.28	$1.32 \times 10^9$	$19.79 \times 10^{-12}$	$3.33 \times 10^{-6}$
Epoxy-E	0.043	$40.36 \times 10^6$	$645.5 \times 10^{-12}$	$108.7 \times 10^{-6}$

#### 4. Conclusions

TMOs of  $ZrO_2:TiO_2:ZnO$  were synthesized via the ball-milling method, and later incorporated into a commercial epoxy polymer (epoxy-TMO) by magnetic stirring and deposited on an SS substrate to reinforce the barrier properties in an aggressive environment of 3.5 wt% NaCl for 28 days. The different characterizations showed that

epoxy-TMO coatings presented different UV absorbance, hydrophilic, and barrier properties, improving the properties of the epoxy coating due to the combination and synergy of the three oxides. After 21 days in the aggressive environment of 3.5 wt% NaCl, the epoxy-D coating, with a TMO composition of 50:40:10, not only showed higher hydrophilic properties, but also presented the highest resistance, in the order of  $\sim 10^{12} \Omega \text{cm}^2$ , with an almost capacitive behavior. Thus, the engineered composition of  $\text{ZrO}_2\text{:TiO}_2\text{:ZnO}$  (50:40:10 wt%) can be considered the ideal candidate for use in organic coatings to reinforce their barrier properties.

**Author Contributions:** Conceptualization, S.V.; methodology, S.V.; validation, S.V., A.F.-A. and H.C.; investigation, S.V., B.B.G., A.A. and G.R.; data curation, A.F.-A. and H.C.; writing—original draft preparation, A.F.-A.; writing—review and editing, A.F.-A., S.V. and H.C.; visualization, A.F.-A.; supervision, S.V. and H.C.; project administration, S.V.; funding acquisition, S.V. All authors have read and agreed to the published version of the manuscript.

**Funding:** Not applicable.

**Institutional Review Board Statement:** Not applicable.

**Informed Consent Statement:** Not applicable.

**Data Availability Statement:** The raw/processed data required to reproduce these findings cannot be shared at this time, as they also form part of an ongoing study.

**Acknowledgments:** A.C. Ferrel-Alvarez, Brenda Galicia, A. Ashk, and G. Regmi wish to thank CONACyT for their postdoctoral and doctoral scholarships.

**Conflicts of Interest:** The authors declare no conflict of interest.

## References

1. Cai, Y.; Quan, X.; Li, G.; Gao, N. Anticorrosion and Scale Behaviors of Nanostructured  $\text{ZrO}_2\text{-TiO}_2$  Coatings in Simulated Geothermal Water. *Ind. Eng. Chem. Res.* **2016**, *55*, 11480–11494. [[CrossRef](#)]
2. Lyon, S.B.; Bingham, R.; Mills, D.J. Advances in corrosion protection by organic coatings: What we know and what we would like to know. *Prog. Org. Coat.* **2017**, *108*, 2–7. [[CrossRef](#)]
3. Ibrahim, M.; Kannan, K.; Parangusan, H.; Eldeib, S.; Shehata, O.; Ismail, M.; Zarandah, R.; Sadasivuni, K.K. Enhanced Corrosion Protection of Epoxy/ZnO-NiO Nanocomposite Coatings on Steel. *Coatings* **2020**, *10*, 783. [[CrossRef](#)]
4. Ma, X.; Peng, C.; Zhou, D.; Wu, Z.; Li, S.; Wang, J.; Sun, N. Synthesis and mechanical properties of the epoxy resin composites filled with sol-gel derived  $\text{ZrO}_2$  nanoparticles. *J. Sol-Gel Sci. Technol.* **2018**, *88*, 442–453. [[CrossRef](#)]
5. Dastgheib, A.; Zarebidaki, A.; Attar, M.M. Enhanced barrier properties of epoxy coating containing  $\text{CaCO}_3$  microparticles modified with cerium nitrate. *Prog. Org. Coat.* **2020**, *144*, 105660. [[CrossRef](#)]
6. González-García, Y.; González, S.; Souto, R.M. Electrochemical and structural properties of a polyurethane coating on steel substrates for corrosion protection. *Corros. Sci.* **2007**, *49*, 3514–3526. [[CrossRef](#)]
7. Pirhady Tavandashiti, N.; Molana Almas, S.; Esmaeilzadeh, E. Corrosion protection performance of epoxy coating containing alumina/PANI nanoparticles doped with cerium nitrate inhibitor on Al-2024 substrates. *Prog. Org. Coat.* **2021**, *152*, 106133. [[CrossRef](#)]
8. Szuch, M. Breadth of dispensing technologies offers a wide variety of conformal coating processing capabilities. *Mater. Sci. IMAPS SoCal* **2004**, 1–13. Available online: [https://www.researchgate.net/publication/237269296\\_Breadth\\_of\\_Dispensing\\_Technologies\\_Offers\\_a\\_Wide\\_Variety\\_of\\_Conformal\\_Coating\\_Processing\\_Capabilities](https://www.researchgate.net/publication/237269296_Breadth_of_Dispensing_Technologies_Offers_a_Wide_Variety_of_Conformal_Coating_Processing_Capabilities) (accessed on 7 February 2022).
9. Aslam, J.; Mobin, M.; Aslam, R.; Ansar, F. Corrosion protection of low carbon steel by conducting terpolymer nanocomposite coating in 3.5 wt% NaCl solution. *J. Adhes. Sci. Technol.* **2020**, *34*, 443–460. [[CrossRef](#)]
10. Al-Daraghme, M.Y.; Hayajneh, M.T.; Almomani, M.A. Corrosion Resistance of  $\text{TiO}_2\text{-ZrO}_2$  Nanocomposite Thin Films Spin Coated on AISI 304 Stainless Steel in 3.5 wt. % NaCl Solution. *Mater. Res.* **2019**, *22*, e20190014. [[CrossRef](#)]
11. Sopicka-Lizer, M. *High Energy Ball Milling: Mechanical Processing of Nano Powders*, Woodhead Publishing Materials; CRC Press: Boca Raton, FL, USA, 2010; pp. 1–5.
12. Velumani, S.; Regmi, G.; Lee, M.; Castaneda, H.; Kuttolamadom, M.; Qian, X.; Kassiba, A. Engineered Zr/Zn/Ti oxide nanocomposite coatings for multifunctionality. *Appl. Surf. Sci.* **2021**, *563*, 150353. [[CrossRef](#)]
13. Pandolfelli, V.C.; Rodrigues, J.A.; Stevens, R. Effects of  $\text{TiO}_2$  addition on the sintering of  $\text{ZrO}_2$ .  $\text{TiO}_2$  compositions and on the retention of the tetragonal phase of zirconia at room temperature. *J. Mat. Sci.* **1991**, *26*, 5327–5334. [[CrossRef](#)]
14. Precious Ayanwale, A.; Reyes-López, S.Y.  $\text{ZrO}_2\text{-ZnO}$  Nanoparticles as Antibacterial Agents. *ACS Omega* **2019**, *4*, 19216–19224. [[CrossRef](#)] [[PubMed](#)]

15. Bavykin, D.V.; Parmon, V.N.; Lapkin, A.A.; Walsh, F.C. The effect of hydrothermal conditions on the mesoporous structure of TiO<sub>2</sub> nanotubes. *J. Mater. Chem.* **2004**, *14*, 3370–3377. [[CrossRef](#)]
16. Deyab, M.A.; Nada, A.A.; Hamdy, A. Comparative study on the corrosion and mechanical properties of nano-composite coatings incorporated with TiO<sub>2</sub> nano-particles, TiO<sub>2</sub> nano-tubes, and ZnO nano-flowers. *Prog. Org. Coat.* **2017**, *105*, 245–251. [[CrossRef](#)]
17. Xia, Y.; Mou, J.; Deng, G.; Wan, S.; Tieu, K.; Zhu, H.; Xue, Q. Sintered ZrO<sub>2</sub>-TiO<sub>2</sub> ceramic composite and its mechanical appraisal. *Ceram. Int.* **2020**, *46*, 775–785. [[CrossRef](#)]
18. Štefanić, G.; Musić, S.; Ivanda, M. Phase development of the ZrO<sub>2</sub>-ZnO system during the thermal treatments of amorphous precursors. *J. Mol. Struct.* **2009**, *924–926*, 225–234. [[CrossRef](#)]
19. Uribe López, M.C.; Alvarez Lemus, M.A.; Hidalgo, M.C.; López González, R.; Quintana Owen, P.; Oros-Ruiz, S.; Uribe López, S.A.; Acosta, J. Synthesis and Characterization of ZnO-ZrO<sub>2</sub> Nanocomposites for Photocatalytic Degradation and Mineralization of Phenol. *J. Nanomater.* **2019**, *2019*, 1015876. [[CrossRef](#)]
20. Simon, S.M.; Chandran, A.; George, G.; Sajna, M.S.; Valparambil, P.; Kumi-Barmiah, E.; Jose, G.; Biju, P.R.; Joseph, C.; Unnikrishnan, N.V. Development of Thick Superhydrophilic TiO<sub>2</sub>-ZrO<sub>2</sub> Transparent Coatings Realized through the Inclusion of Poly(methyl methacrylate) and Pluronic-F127. *ACS Omega* **2018**, *3*, 14924–14932. [[CrossRef](#)] [[PubMed](#)]
21. DeBakker, C.J.; George, G.A.; St. John, N.A.; Fredericks, P.M. The kinetics of the cure of an advanced epoxy resin by Fourier transform Raman and near-IR spectroscopy. *Spectrochim. Acta A Mol. Spectrosc.* **1993**, *49*, 739–752. [[CrossRef](#)]
22. Nikafshar, S.; Zabihi, O.; Ahmadi, M.; Mirmohseni, A.; Taseidifar, M.; Naebe, M. The Effects of UV Light on the Chemical and Mechanical Properties of a Transparent Epoxy-Diamine System in the Presence of an Organic UV Absorber. *Materials* **2017**, *10*, 180. [[CrossRef](#)] [[PubMed](#)]
23. Xu, H.; Liu, W.; Cao, L.; Su, G.; Duan, R. Preparation of porous TiO<sub>2</sub>/ZnO composite film and its photocathodic protection properties for 304 stainless steel. *Appl. Surf. Sci.* **2014**, *301*, 508–514. [[CrossRef](#)]
24. Horti, N.C.; Kamatagi, M.D.; Nataraj, S.K.; Wari, M.N.; Inamdar, S.R. Structural and optical properties of zirconium oxide (ZrO<sub>2</sub>) nanoparticles: Effect of calcination temperature. *Nano Express* **2020**, *1*, 010022. [[CrossRef](#)]
25. Sathyaseelan, B.; Manikandan, E.; Baskaran, I.; Senthilnathan, K.; Sivakumar, K.; Moodley, M.K.; Ladchumananandasivam, R.; Maaza, M. Studies on structural and optical properties of ZrO<sub>2</sub> nanopowder for opto-electronic applications. *J. Alloys Comp.* **2017**, *694*, 556–559. [[CrossRef](#)]
26. Xie, Y.; Jiang, Y.; Zhao, S. Improving the wettability on ZnO and ZrO<sub>2</sub> single crystal surface by laser irradiation. *J. Laser Appl.* **2012**, *2012*, 943–946.
27. Nikoomezari, E.; Fattah-alhosseini, A.; Pajohi Alamoti, M.R.; Keshavarz, M.K. Effect of ZrO<sub>2</sub> nanoparticles addition to PEO coatings on Ti–6Al–4V substrate: Microstructural analysis, corrosion behavior and antibacterial effect of coatings in Hank's physiological solution. *Ceram* **2020**, *46*, 13114–13124. [[CrossRef](#)]
28. Banerjee, S.; Dionysiou, D.D.; Pillai, S.C. Self-cleaning applications of TiO<sub>2</sub> by photo-induced hydrophilicity and photocatalysis. *Appl. Catal. B* **2015**, *176–177*, 396–428. [[CrossRef](#)]
29. Sanu, M.S.; Chandran, A.; Prakashan, V.P.; George, G.; Sajna, M.S.; Biju, P.R.; Joseph, C.; Unnikrishnan, N.V. Synthesis and hydrophilic mechanism of porous TiO<sub>2</sub>-ZrO<sub>2</sub> transparent coatings. *AIP Conf. Proceed.* **2019**, *2082*, 030031. [[CrossRef](#)]
30. Elkebir, Y.; Mallarino, S.; Trinh, D.; Touzain, S. Effect of physical ageing onto the water uptake in epoxy coatings. *Electrochim. Acta* **2020**, *337*, 135766. [[CrossRef](#)]
31. Ghomi, R.; Khorasani, S.N.; Koochaki, S.; Dinari, M.; Ataei, S.; Enayati, M.H.; Das, O.; Neisiany, R.E. Synthesis of TiO<sub>2</sub> nanogel composite for highly efficient self-healing epoxy coating. *J. Adv. Res.* **2022**, *1–10*, In Press. [[CrossRef](#)]
32. Xavier, J.R.; Nallaiyan, R. Application of EIS and SECM studies for investigation of anticorrosion properties of epoxy coatings containing ZrO<sub>2</sub> nanoparticles on mild steel in 3.5% NaCl solution. *J. Fail. Anal. Preven.* **2016**, *16*, 1082–1091. [[CrossRef](#)]
33. Rostami, M.; Rasouli, S.; Ramezanzadeh, B.; Askari, A. Electrochemical investigation of the properties of Co doped ZnO nanoparticle as a corrosion inhibitive pigment for modifying corrosion resistance of the epoxy coating. *Corros. Sci.* **2014**, *88*, 387–399. [[CrossRef](#)]
34. Harb, S.V.; Trentin, A.; Uvida, M.C.; Magnani, M.; Pulcinelli, S.H.; Santilli, C.V.; Hammer, P. A comparative study on PMMA-TiO<sub>2</sub> and PMMA-ZrO<sub>2</sub> protective coatings. *Prog. Org. Coat.* **2020**, *140*, 105477. [[CrossRef](#)]
35. Golnaz, N.A.; Arvin, T.T.; Aghajani, H. Investigation on corrosion behavior of Cu-TiO<sub>2</sub> nanocomposite synthesized by the use of SHS method. *J. Mater. Res. Technol.* **2019**, *8*, 22116–22222. [[CrossRef](#)]